entropy

MDPI

Article

Entropy Generation and Heat Transfer Performances of Al_2O_3-Water Nanofluid Transitional Flow in Rectangular Channels with Dimples and Protrusions

Yonghui Xie [1,*], Lu Zheng [1], Di Zhang [2] and Gongnan Xie [3]

1 School of Energy and Power Engineering, Xi'an Jiaotong University, Xi'an 710049, China; water.element@stu.xjtu.edu.cn

2 Key Laboratory of Thermo-Fluid Science and Engineering, Ministry of Education, School of Energy and Power Engineering, Xi'an Jiaotong University, Xi'an 710049, China; zhang_di@mail.xjtu.edu.cn

3 Department of Mechanical and Power Engineering, School of Marine Science and Technology, Northwestern Polytechnical University, Xi'an 710072, China; Gongnan.Xie@gmail.com

* Correspondence: yhxie@mail.xjtu.edu.cn; Tel.: +86-29-8266-4443

Academic Editors: Giulio Lorenzini and Omid Mahian

Received: 25 February 2016; Accepted: 13 April 2016; Published: 19 April 2016

Abstract: Nanofluid has great potentials in heat transfer enhancement and entropy generation decrease as an effective cooling medium. Effects of Al_2O_3-water nanofluid flow on entropy generation and heat transfer performance in a rectangular conventional channel are numerically investigated in this study. Four different volume fractions are considered and the boundary condition with a constant heat flux is adopted. The flow Reynolds number covers laminar flow, transitional flow and turbulent flow. The influences of the flow regime and nanofluid volume fraction are examined. Furthermore, dimples and protrusions are employed, and the impacts on heat transfer characteristic and entropy generation are acquired. It is found that the average heat transfer entropy generation rate descends and the average friction entropy generation rate rises with an increasing nanofluid volume fraction. The effect of nanofluid on average heat transfer entropy generation rate declines when Reynolds number ascends, which is inverse for average friction entropy generation rate. The average wall temperature and temperature uniformity both drop accompanied with increasing pumping power with the growth in nanofluid volume fraction. The employment of dimples and protrusions significantly decreases the average entropy generation rate and improve the heat transfer performance. The effect of dimple-case shows great difference with that of protrusion-case.

Keywords: nanofluid; convection heat transfer; entropy generation; transitional flow; dimples and protrusions

1. Introduction

As the remarkable development of the electronic equipment technology and consequent continuous growth of the device output power, the requirement of superior cooling technique has been dramatically drawing the researchers' attention. Due to limited cooling capacity of the conventional working substance, it is unable to meet the highly demanding cooling requirement. In the past few years, the nanofluids cooling technology has emerged since the higher thermal conductivities compared with the base fluids, and it has great potential in heat transfer enhancement as a promising cooling medium.

Choi [1] defined the dilute suspensions in which nano-sized particles are dispersed in traditional liquids as "nanofluids" in which the nanoparticles cover metals, metal-oxides, polymers, silica or even carbon nanotubes and the base fluids generally include water, oil, or ethylene glycol. Saidur *et al.* [2]

discussed the various applications of nanofluids and listed the challenges of nanofluids in thermal engineering systems applications. A great number of investigations have been conducted on nanofluids thermophysical properties. Haddad *et al.* [3] numerically and experimentally investigated the natural convection of nanofluids in various types of cavities. Khanafer and Vafai [4] examined published models for calculating nanofluids thermophysical properties, mainly including thermal conductivity, viscosity, specific heat, and density. Mahbubul *et al.* [5] accomplished a comparison of different effective models for the viscosity of nanofluids. Fan and Wang [6] provided a review on heat conduction of nanofluids in which they focused on thermal conductivity of nanofluids. Brinkman [7] obtained an expression for predicting viscosities of solutions and suspensions within finite concentrations, and the influence of the additional one solute-molecule was taken into consideration. The Brinkman model was obtained as the most common relation that has been used to calculate the viscosity in the entropy generation problems. Corcione [8] carried out a theoretical investigation on the heat transfer characteristics of buoyancy-driven nanofluids in rectangular enclosures with vertical walls heated discriminately and presented an empirical correlation by regression analysis of experimental data. Duangthongsuk and Wongwises [9] experimentally examined the viscosity and thermal conductivity of nanofluids where TiO_2 nanoparticles are dispersed in water, based on which the expressions for predicting the viscosity of TiO_2-water nanofluids were presented. The Maxwell model [10] is one of the earliest approaches to calculate the thermal conductivity of solid-liquid mixtures. Bruggeman [11] presented a thermal conductivity model considering interactions among the spherical particles, which can be used for high quantities of particle loadings of nanoparticles with in spherical shape. Hamilton and Crosser [12] carried out an investigation on the effect of included nanoparticle shape, composition, and pure component on the thermal conductivity of various two-component mixtures composed by continuous and discontinuous phases. They acquired a modified Maxwell model by taking the shape of nanoparticles into consideration. Nan *et al.* [13] proposed a methodology on the evaluation of the effective thermal conductivity of the arbitrary particulate composite. Based on the effective medium approach, the interfacial thermal resistance is considered, and the essential concept of Kapitza thermal contact resistance is also taken into account. A good agreement was found in the comparison of the results predicted with the existing models and experimental results. Taking the effect of the nanolayer between the liquid molecules and solid surface into consideration, the Maxwell model for predicting thermal conductivities has been modified by Yu and Choi [14] and a renovated Maxwell model was obtained. Then, they [15] proposed a renovated Hamilton–Crosser model that can be employed for nonspherical particles. With the renovated model, a correct prediction of the magnitude of the thermal conductivity of nanotube-in-oil nanofluids was acquired. Koo and Kleinstreuer [16] presented a model for calculating the thermal conductivity of nanofluids (K-K model) and they took account of the influences of the particle size, volume fraction and temperature dependence, and effects of the properties of base fluid and nanoparticles are also seriously considered. Feng and Kleinstreuer [17] proposed a more advanced theory that was free of any matching function or coefficient (F-K model), based on an analogy between the random nanoparticle fluctuations generated by the Brownian motion effect and turbulent fluctuations. Considering the extended irreversible thermodynamics, Machrafi and Lebon [18] presented a model for predicting nanofluids thermal conductivities, and the effect of coupled heat transfer mechanisms is taken into great consideration, including the interfacial layering between the base fluid and nanoparticles, Brownian motion and particles agglomeration. Besides, an assessment of the effect on the thermal conductivity of each mechanism was given.

Besides, a large number of studies on convective heat transfer enhancement by nanofluids have also been accomplished. Seyf and Feizbakhshi [19] carried out a numerical investigation on the application of nanofluids in Micro-Pin-Fin Heat Sinks. De-ionized water was selected to be the base fluid and the nanoparticles employed were CuO and Al_2O_3 nanoparticles with different mean diameters. Selvakumar and Suresh [20] conducted a study on the convective heat transfer of CuO-water nanofluids and a thin-channeled copper water block was adopted. Diao *et al.* [21] achieved a research on the heat transfer characteristic of a microchannel surface at different pressures, and the effect of

Al_2O_3-R141b nanofluids with various particle concentrations was considered. Wen and Ding [22] conducted a study on the convective heat transfer of γ-Al_2O_3-deionized water nanofluids in a copper tube under laminar flow. Suresh *et al.* [23] experimentally examined the convective heat transfer and friction characteristics of distilled water and CuO-water nanofluids in flat and dimpled tube under laminar flow, and a constant heat flux boundary condition was adopted. Later on, they conducted a similar study under turbulent flow [24]. Vakili *et al.* [25] completed a research on the heat transfer behavior of TiO_2 nanofluid with different nanoparticle concentrations in a vertical pipe at different constant heat fluxes. Xuan and Li [26] built an experimental system to investigate the convective heat transfer and flow characteristics of nanofluids in a tube, acquiring a new convective heat transfer correlation for correlating experimental data of nanofluids. Gavili *et al.* [27] conducted a study on the heat transfer and flow characteristics of Al_2O_3-water nanofluid in a two-sided lid-driven rectangular cavity with walls heated discriminately. Mohammed *et al.* [28] achieved an investigation on the heat transfer and flow characteristics of nanofluids in a channel with ribs and grooves under turbulent flow. Nanoparticles, Al_2O_3, CuO, SiO_2, and ZnO, and base fluids, water, glycerin, and engine oil, are all examined, respectively. Besides, the effects of the volume fraction and nanoparticle diameter are further studied.

Furthermore, except for enhancing the convection heat transfer as much as possible, it is also of significant importance to reduce the entropy generation to the greatest extent. Entropy generation determines the level of irreversibility accumulation during the flow and heat transfer process. Consequently, entropy generation is usually used for evaluating the performance of engineering devices. Oztop and Al-Salem [29] reported a review on the entropy generation in natural and mixed convection heat transfer in energy systems. Singh *et al.* [30] theoretically investigated the effect on entropy generation of Al_2O_3-water nanofluid in channels in three different sizes containing microchannels, minichannels, and conventional channels. The results under laminar flow and turbulent flow are both considered, and a prediction of the entropy generation rate was provided through an order of magnitude approach. Li and Kleinstreuer [31] numerically studied the entropy generation of CuO-water nanofluid in trapezoidal microchannels. The volume fractions lower than 4% and steady laminar developing flow are employed. Moghaddami *et al.* [32] presented an estimation of the entropy generation of Al_2O_3-water and Al_2O_3-EG nanofluids in a circular tube under both laminar and turbulent flows using a constant heat flux boundary condition. Leong *et al.* [33] studied the entropy generation of TiO_2-water and Al_2O_3-water nanofluids flows in a circular tube with a wall at constant temperature. Mahian *et al.* [34] conducted an investigation on the entropy generation due to nanofluids between two isoflux rotating cylinders and two types of nanofluids, Al_2O_3-EG and TiO_2-water, were considered. Shahi *et al.* [35] conducted a numerical investigation on the entropy generation of Cu-water nanofluids in a square cavity with four different designs, where a heat source was arranged. Mahmoudi *et al.* [36] considered the entropy generation of Cu-water nanofluid natural convection in a cavity, in which three walls were set as adiabatic, and a constant temperature was employed on the right wall. Khorasanizadeh *et al.* [37] carried out an investigation on the entropy generation of Cu-water nanofluids in a square cavity where the top wall moved with an invariable velocity and the bottom wall was set as adiabatic. Khorasanizadeh *et al.* [38] also finished a research on the entropy generation inside a cavity where a baffle is arranged on the bottom hot surface. Esmaeilpour and Abdollahzadeh [39] reported a study on the entropy generation of Cu-water nanofluids natural convection in a cavity with wavy walls. Cho *et al.* [40] conducted an investigation on natural convection of water-based nanofluids in an enclosure with wavy walls, and three different types of nanoparticles, Cu, Al_2O_3 and TiO_2, are adopted, respectively. Boghrati *et al.* [41] achieved a numerical investigation on the entropy generation of the Al_2O_3-water and carbon nanotubes-water nanofluids flows through two horizontal parallel plates with a rectangular barrier. Sarkar *et al.* [42] conducted a study on the entropy generation of water-based Al_2O_3 and Cu nanofluids mixed convection flowing past a square barrier in the middle of two parallel plates. Leong *et al.* [43] carried out an investigation on the heat transfer performance of Cu-water nanofluids in three types of shell-and-tube heat exchangers.

Matin *et al.* [44] accomplished a numerical research on MHD mixed convection flow using SiO_2-water nanofluids over a non-linear stretching sheet. Selimefendigil *et al.* [45] carried out an investigation on entropy generation of nanofluids natural convection in entrapped trapezoidal cavities taking the influence of magnetic field into consideration.

According to Singh *et al.* [30], from the view point of decreasing entropy generation, the Al_2O_3-water nanofluids behaves better in conventional channels and minichannels under laminar flow, and similar behavior can be found in minichannels and microchannels under turbulent flow, which indicates the significant influences of nanofluids flow regime and channel size on entropy generation. Furthermore, dimples and protrusions are two excellent types of passive flow control turbulator, which are widely used in the current heat transfer augment technique and have great heat transfer enhancement capacity without excessive additional flow resistance penalty. In the present paper, the heat transfer performance and flow characteristics of Al_2O_3-water nanofluid at four different volume fractions in a rectangular conventional channel with dimples and protrusions are numerically investigated. The different flow regimes are considered including laminar flow, turbulent flow and transitional flow. The effects of the nanofluid volume fraction and dimples/protrusions on entropy generation and heat transfer performance are obtained. Both heat transfer entropy generation and friction entropy generation are taken into consideration. Besides, the effects on average wall temperature, wall temperature uniformity and pumping power are also analyzed to provide assessments of the thermal performance.

2. Physical Model and Numerical Methods

2.1. Physical Model and Numerical Method

In this study, the heat transfer performance and entropy generation characteristic of the Al_2O_3-water nanofluid flow in a conventional rectangular channel with staggered dimples or protrusions are numerically studied. Figure 1 shows the schematic diagram of the flow domain in this paper. The x, y, z represent the streamwise direction, spanwise direction and normal direction, respectively. The whole calculation domain consists of three parts, and the investigated part that is the middle heated section of the domain has a length of L = 245 mm. An inlet extension and an outlet extension, both of which are long enough, are set at the inlet and outlet, respectively, to guarantee a fully developed flow and avoid the outlet effect. The width W and height H of the flow channel are 125 mm and 10 mm, respectively. The staggered dimples or protrusions are arranged on one side of the channel. The detailed geometric parameters of dimples and protrusions are given in Figure 2. As two of the most important parameters of dimple or protrusion structure, the print diameter D = 30 mm while the ratio of depth-to-print diameter δ/D is 0.2. All dimples or protrusions are uniformly distributed on the heated surface, and the opposite side is also heated with a constant flux of 50,000 W/m^2 while the other walls are adiabatic. All the walls are set to be nonslip boundary in the computation. The flow Reynolds number Re ranges from 1000 to 40,000. Fully developed velocity boundary is employed on inlet, and the outlet pressure is set as the atmospheric pressure. The detailed information about the turbulator structures and nanofluid volume fractions of all cases are shown in Table 1.

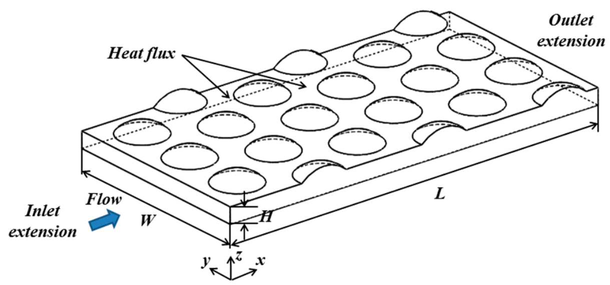

Figure 1. Schematic diagram and detailed information of the flow domain.

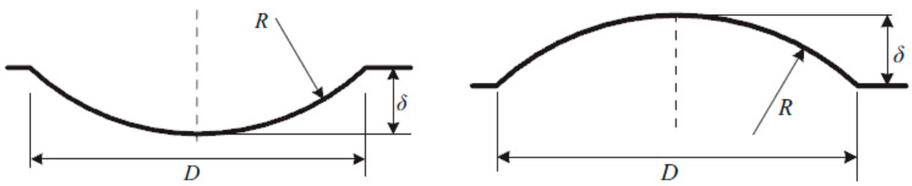

Figure 2. Detailed geometric parameters of dimples and protrusions.

Table 1. Detailed information of the cases.

Case	**Turbulator Structure**	**Volume Fraction (ϕ)**	**Case**	**Turbulator Structure**	**Volume Fraction (ϕ)**	***Re***
Case 1	dimples	0%	Case 5	protrusions	0%	1000~40,000
Case 2	dimples	3%	Case 6	protrusions	3%	1000~40,000
Case 3	dimples	6%	Case 7	protrusions	6%	1000~40,000
Case 4	dimples	9%	Case 8	protrusions	9%	1000~40,000

The 3D Navier–Stokes (NS) equations in steady form are solved through the finite-volume based computational fluid dynamics solver CFX (version 15.0) to obtain the flow and heat transfer characteristic. The assumption that the flow is three-dimensional, steady, and incompressible is employed and the constant physical property is adopted. The resulting conservation equations of mass, momentum, and energy are given as follows

$$\frac{\partial \rho u_i}{\partial x_i} = 0 \tag{1}$$

$$\frac{\partial \rho u_i u_j}{\partial x_i} = \rho g_i + F_i - \frac{\partial P}{\partial x_i} + \frac{\partial}{\partial x_i}(2\mu S_{ij}) \tag{2}$$

$$\frac{\partial \rho u_i E_0}{\partial x_i} = \rho u_i F_i - \frac{\partial q_i}{\partial x_i} + \frac{\partial}{\partial x_i}(u_i T_{ij}) \tag{3}$$

The NS equations are solved with implicit coupling method, the second order central differential scheme is employed in the diffusion term discretization and the advection discretization is achieved using high resolution scheme. The residues of continuity, energy and velocities are monitored to provide the judgment of the convergence of the computation, where the convergence criteria is set as 1×10^{-6}. Besides, the temperature and velocity at the monitoring point are considered to judge the convergence of the computations in addition.

Considering the present Reynolds number range, which may cover laminar flow, transitional flow and turbulent flow, it is greatly appropriate to employ the shear stress transport (SST) turbulence model [46] coupled with Gamma-Theta transition model [47] as an effective approach to deal with the transitional flow in the present study. The transport equations of intermittency γ and transition momentum thickness Reynolds number $Re_{\theta t}$ are given as follows

$$\frac{\partial(\rho\gamma)}{\partial t} + \frac{\partial(\rho u_i \gamma)}{\partial x_i} = P_{\gamma 1} - E_{\gamma 1} + P_{\gamma 2} - E_{\gamma 2} + \frac{\partial}{\partial x_i}\left[\left(\mu + \frac{\mu_t}{\sigma_f}\right)\frac{\partial \gamma}{\partial x_i}\right] \tag{4}$$

$$\frac{\partial(\rho \mathrm{Re}_{\theta t})}{\partial t} + \frac{\partial(\rho u_i \mathrm{Re}_{\theta t})}{\partial x_i} = P_{\theta t} + \frac{\partial}{\partial x_i}\left[\sigma_{\theta t}\left(\mu + \mu_t\right)\frac{\partial \mathrm{Re}_{\theta t}}{\partial x_i}\right] \tag{5}$$

where $P_{\gamma 1}$ and $E_{\gamma 1}$ are the transition sources, and $P_{\gamma 2}$ and $E_{\gamma 2}$ are the destruction sources. μ and μ_t are the molecular viscosity coefficient and eddy viscosity coefficient. $P_{\theta t}$ stands for the source term of the transition momentum thickness Reynolds number. The production terms of the turbulent kinetic energy downstream of the transition point is turned on by the employment of the intermittency. The empirical correlations are induced by the transition momentum thickness Reynolds number; besides, the influences of the turbulence kinetic energy in the freestream and adverse pressure gradient are also captured. The transition model is realized based on the local variables, which can be easily achieved with the help of current CFD methods. Furthermore, the transition model is able to provide predictions of various transition processes using proper correlations based on experimental data, and the simulation results will be more reliable and accurate with the improvement of the correlation. The transition model coupled with SST turbulence model is adopted in this study.

2.2. Physical Property of Nanofluid

In the present study, the Al_2O_3-water nanofluids consisting of water as base fluid and Al_2O_3 spherical nanoparticle with 30 nm diameter is employed. It is assumed that there is no motion slip between the continuous liquid and the discontinuous phase of the dispersed nanoparticles. Besides, it is also adopted that the local thermal equilibrium between base fluid and nanoparticles is achieved. Furthermore, the nanofluid is assumed to be in single phase [48] to evaluate the effective physical properties, including density, specific heat, dynamic viscosity and thermal conductivity. The effective models are given by:

- Density model ρ:

$$\rho_{nf} = (1-\phi)\rho_f + \phi\rho_p \tag{6}$$

- Specific heat model C_p [49]:

$$(\rho C_p)_{nf} = (1-\phi)(\rho C_p)_f + \phi(\rho C_p)_p \tag{7}$$

- Brinkman viscosity model μ [7], which is the most common relation to calculate the viscosity in the entropy generation problems:

$$\mu_{nf} = \frac{\mu_f}{(1-\phi)^{2.5}} \tag{8}$$

- Bruggeman thermal conductivity model k [11] that can be applied to spherical particle with various concentrations:

$$\frac{k_{nf}}{k_f} = \frac{(3\phi-1)\frac{k_p}{k_f} + \{3(1-\phi)-1\} + \sqrt{\Delta}}{4} \tag{9}$$

where

$$\Delta = \left[(3\phi-1)\frac{k_p}{k_f} + \{3(1-\phi)-1\}\right]^2 + 8\frac{k_p}{k_f} \tag{10}$$

In this paper, four different volume fractions are employed: 0%, 3%, 6% and 9%, to investigate the influence of volume fraction. The effective physical property models above are valid within the volume fraction range considered in this study.

2.3. Data Reduction

The flow Reynolds number Re in the present paper is defined by

$$\mathrm{Re} = \frac{\rho U_{m,in} D_h}{\mu} \tag{11}$$

where $U_{m,in}$ stands for the average inlet velocity. The hydraulic diameter D_h is defined as

$$D_h = \frac{2WH}{W+H} \tag{12}$$

The pumping power $P.P$ can be calculated as follows:

$$P.P = \frac{M}{\rho} \cdot \Delta P \tag{13}$$

where ΔP is the pressure drop between the inlet and outlet of the flow domain, and M represents the mass flow rate. The temperature uniformity ΔT_s is given as follow, indicating the temperature distribution uniformity on the heated surface

$$\Delta T_s = T_{w,\max} - T_{w,\min} \tag{14}$$

where $T_{w,max}$ and $T_{w,min}$ are the maximum and minimum temperature of the heated wall, respectively. The heated wall average temperature T_w is defined by

$$T_w = \frac{\int T dA}{A} \tag{15}$$

where A represents the area of the heated wall. Besides, the Nusselt number Nu and flow resistance coefficient f are given as follows, which are employed in the method validation and grid independence study section

$$Nu = \frac{hD_h}{k},\ f = \frac{2(\Delta P/L)D_h}{\rho U_{m,in}} \tag{16}$$

where h is the heat transfer coefficient and $\Delta P/L$ is the pressure gradient along the streamwise.

According to the relevant published literature, the local entropy generation rate S'''_{gen} in Cartesian coordinate systems can be obtained using the following relations [50]

$$\begin{aligned} S'''_{gen} = S'''_h + S'''_f = \tfrac{k}{T^2}\left[(\tfrac{\partial T}{\partial x})^2 + (\tfrac{\partial T}{\partial y})^2 + (\tfrac{\partial T}{\partial z})^2\right] \\ + \tfrac{\mu}{T}\left\{2\left[(\tfrac{\partial v_x}{\partial x})^2 + (\tfrac{\partial v_y}{\partial y})^2 + (\tfrac{\partial v_z}{\partial z})^2\right] + (\tfrac{\partial v_x}{\partial y} + \tfrac{\partial v_y}{\partial x})^2 + (\tfrac{\partial v_x}{\partial z} + \tfrac{\partial v_z}{\partial x})^2 + (\tfrac{\partial v_y}{\partial z} + \tfrac{\partial v_z}{\partial y})^2\right\} \end{aligned} \tag{17}$$

where the first term S'''_{h} and second term S'''_{f} on the right hand stand for the local entropy generation rates due to the heat transfer and flow friction, respectively. Through the numerical simulation, the local entropy generation rate can be obtained at every point in the flow domain. Furthermore, the total entropy generation can be obtained through the integral of the local entropy generation rate distribution over the whole domain. It can be found from Equation (17) that thermal conductivity and viscosity have significant influences on the entropy generation. The physical properties of nanofluids should be used in the equation above for the present study. Then, the average total entropy generation rate S_{rgen} is given by

$$S_{rh} = \frac{\int S'''_h dV}{V},\ S_{rf} = \frac{\int S'''_f dV}{V},\ S_{rgen} = S_{rh} + S_{rf} \tag{18}$$

where S_{rh} and S_{rf} are the average heat transfer entropy generation rate and average friction entropy generation rate, respectively. The dimensionless local entropy generation rate S'''_{dgen} is defined as

$$S'''_{dgen} = S'''_{dh} + S'''_{df} = \frac{S'''_h}{S_{rh0}} + \frac{S'''_f}{S_{rf0}} \tag{19}$$

where S'''_{dh} and S'''_{df} are the dimensionless local heat transfer entropy generation rate and dimensionless local friction entropy generation rate, respectively. S_{rh0} and S_{rf0} are the average heat transfer entropy generation rate and average friction entropy generation rate of the smooth channel without dimples or protrusions.

2.4. Method Validation and Grid Independence Study

In order to guarantee the validity of the method in the present study, a numerical method validation is completed through the comparison between the results in this study and other published results, as shown in Figure 3. It is shown that, considering the Re range in which Gnielinski [51] is valid, the present Nusselt numbers are in agreement with those based on Gnielinski when Re is no less than 3000. Besides, the Nusselt numbers at Re = 1000 and 3000 are in accordance with that of Shah [52]. It is found from Figure 3b that the f values in the present study agree with those from Filonenko [53]. In conclusion, the present method is deemed to be valid for predicting the flow and heat transfer in this study. Moreover, Gnielinski and Shah Equations are given as follows, as well as Filonenko Equation.

- Gnielinski:

$$Nu = \frac{(f/8)(Re - 1000)Pr_f}{1 + 12.7\sqrt{f/8}(Pr_f^{2/3} - 1)}[1 + \left(\frac{D_h}{L}\right)^{2/3}]c_t \tag{20}$$

where $c_t = \left(\frac{Pr_f}{Pr_w}\right)^{0.01}$, f is given as Filonenko Equation and L is the length of the domain considered. Pr_f and Pr_w are the Prandtl numbers based on the average fluid temperature and wall temperature, respectively.

- Filonenko:

$$f = (1.82\mathrm{lg}Re - 1.64)^{-2} \tag{21}$$

- Shah:

$$Nu = 1.953\left(RePr\frac{D_h}{L}\right)^{1/3} \tag{22}$$

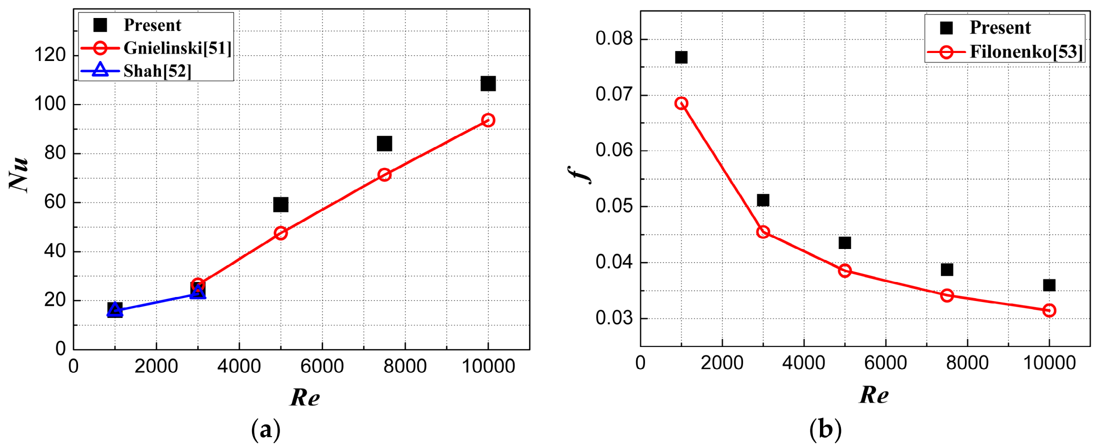

Figure 3. Validation of the present method: (**a**) *Nu vs. Re*; and (**b**) *f vs. Re*.

All hexahedral mesh is adopted in this study and the y^+ in all cases is less than 1 to guarantee the computation precision. The O-type block mesh is employed near the dimples and protrusions in order to improve the local mesh quality. In order to achieve a balance between the calculation precision and computational resource, a grid independence study is carried out to obtain the reasonable grid for computation. As is shown in Table 2, the relative discrepancies of Nu and f are 0.566% and 0.603% when the mesh changes from Mesh 3 to Mesh 4, respectively. Therefore, the proposed mesh is Mesh 3.

Table 2. Grid independence study.

Mesh	Grid Number (million)	*Nu*	Difference (%)	$f \times 10^2$	Difference (%)
Mesh 1	0.582	73.467	7.367	6.634	8.134
Mesh 2	1.496	70.235	2.644	6.383	4.042
Mesh 3	2.889	68.813	0.566	6.172	0.603
Mesh 4	4.541	68.426	Reference	6.135	Reference

3. Results and Discussion

The Reynolds number in this paper ranges from 1000 to 40,000, which covers laminar flow, transitional flow and turbulent flow. After checking the turbulence intermittency of all cases, it is found that when *Re* reaches 10,000 or higher, the flow has successfully turned into fully developed turbulent flow. Moreover, the variation tendencies of entropy generation and other relevant parameters in the cases with *Re* at 10,000 or higher show no aberrations or unpredictable changes. In other words, the variation tendency of the considered parameters when *Re* is no less than 10,000 is in correspondence with that when *Re* ranges 1000 from 10,000. Thus, for a more distinct understanding of the results and discussion, this section provides the illustration and explanation of the cases with *Re* from 1000 to 10,000.

3.1. Flow Regimes and Flow Structures

Considering the focus of this paper-the entropy generation and heat transfer characteristics near the transitional flow, it is necessary to give an estimate about the flow regimes at different Reynolds number based on the simulation results. Taking the cases with nanofluids volume fraction at 0% as examples, the turbulence intermittency γ distributions contour and streamlines on the middle plane vertical to the spanwise are shown in Figure 4, where the legend levels are mandatorily set from 0 to 1 and the mainstream flows from the left to right. When γ equals to 0, the flow regime is considered to be laminar flow, and it is supposed to be turbulent flow when γ is 1. The flow with γ between 0 and 1 is defined as the transitional flow. It is shown that when *Re* = 1000, the mainstream is principally considered to be under laminar flow, and with the growth in *Re*, the turbulivity gets more intensified especially at the center of dimples and back porch of protrusions. When *Re* = 5000, the turbulent flow almost occupies the major part of the domain and the laminar flow only exists at the flow boundary layers neat the wall, leading to a laminar-layer. With the further increase in *Re*, the thickness of the laminar-layer keeps continuously declining. It can be concluded that when *Re* reaches 10,000 or even higher, the mainstream has completely turned into turbulent flow, and the Reynolds number range in this study covers laminar flow, transitional flow and turbulent flow. The cases with Reynolds numbers higher than 10,000 are additionally accomplished to study the influence of higher *Re*, which may better meet the practical industrial requirement.

With regard to the flow structures, a large flow separation region occurs inside the dimple when *Re* = 1000 which occupies the major section of the dimple, and the core of the vortex gradually moves towards the dimple center with the rise in *Re*. In protrusion cases, there is a large separation region at the protrusion trailing edge and the reattachment turns up at the leading edge of the adjacent protrusion. When *Re* ascends, the flow separation region size slightly increases. There exists a dense-streamline region near the protrusion top, indicating a local high velocity region.

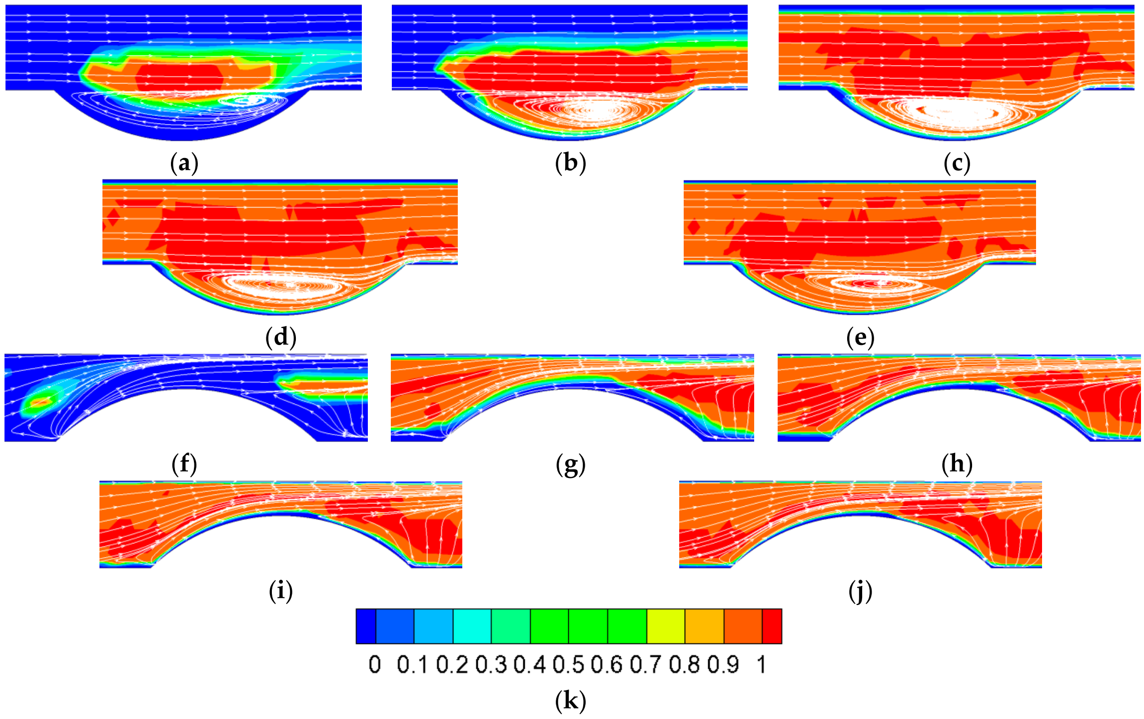

Figure 4. Turbulence intermittency γ distributions contour and streamlines on the middle plane: (**a**) dimple-*Re* = 1000; (**b**) dimple-*Re* = 3000; (**c**) dimple-*Re* = 5000; (**d**) dimple-*Re* = 7500; (**e**) dimple-*Re* = 10,000; (**f**) protrusion-*Re* = 1000; (**g**) protrusion-*Re* = 3000; (**h**) protrusion-*Re* = 5000; (**i**) protrusion-*Re* = 7500; (**j**) protrusion-*Re* = 10,000; (**k**) color guide for (a–j).

3.2. Entropy Generation Analysis

3.2.1. Effect of Nanofluids on Entropy Generation

The variation tendencies of average heat transfer entropy generation rate S_{rh} and average friction entropy generation rate S_{rf} with *Re*, as well as the average total entropy generation rate S_{rgen}, are shown in Figure 5a,c,e. Furthermore, the entropy generation differences of S_{rh}, S_{rf} and S_{rgen} due to the nanofluid with *Re* are given in Figure 5b,d,f, respectively. It can be found in Figure 5a that S_{rh} values in all cases observably decrease with the increase in *Re*, and the slopes get increasingly lower when *Re* rises, indicating the weaker influence to S_{rh} of *Re* when flow velocity ascends. Furthermore, from the viewpoint of the effect of nanofluids, it can apparently be seen that the employment of nanofluid markedly reduces the S_{rh} values in all Reynolds numbers in both dimple-case and protrusion-case. The S_{rh} value keeps decreasing at a given Reynolds number with an increasing volume fraction. It should be noted that the decrease of the S_{rh} value owing to nanofluids declines with the increase in *Re*. Taking the S_{rh} value differences between the cases with ϕ = 0% and ϕ = 9% as examples (Figure 5b), the decrease extent dramatically descends with the growth in *Re*, from about 550 when *Re* = 1000 to about 100 when *Re* = 10,000 for dimple-case, which keeps dropping when *Re* further grows. The results above can be explained by that due to the high thermal conductivity of nanofluid, the physical property has great effects on the heat transfer performance when the mainstream keeps in laminar flow with low *Re*, which signally enhances the local heat transfer and decrease the local temperature gradient, leading to a lower heat transfer entropy generation rate. With the increase in *Re*, the mainstream gradually turns into turbulent flow, and the turbulence acts as the predominant impetus in heat transfer enhancement. The effect of the nanofluid thermal conductivity is not as significant as that when *Re* is low. As a result, the effect of nanofluids relatively weakens.

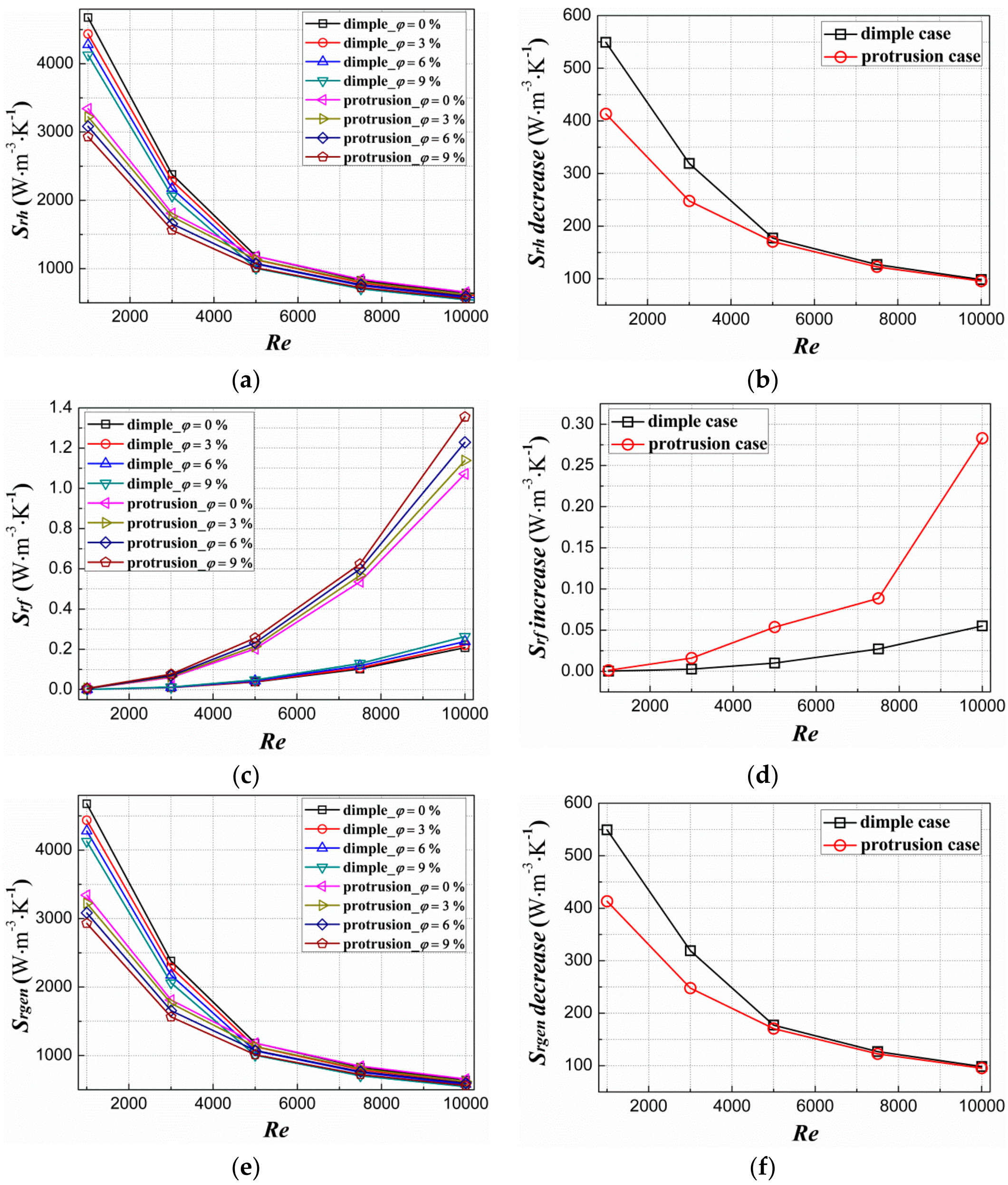

Figure 5. Average entropy generation rate characteristic: (**a**) S_{rh} *vs. Re*; (**b**) S_{rh} decrease *vs. Re*; (**c**) S_{rf} *vs. Re*; (**d**) S_{rf} increase *vs. Re*; (**e**) S_{rgen} *vs. Re*; and (**f**) S_{rgen} decrease *vs. Re*.

On the contrary, S_{rf} value exhibits an opposite variation tendency. It can be found from Figure 5c that the S_{rf} values in all cases observably ascend with the increase in *Re*, and the S_{rf} values rise faster when *Re* is higher, which suggests that the influence on S_{rf} of *Re* gets increasingly significant with higher *Re*. From the view point of nanofluid effect, the employment of nanoparticles increases the S_{rf} values in both dimple-case and protrusion-case at a given *Re*, and S_{rf} ascends with an increasing volume fraction, which is mainly caused by the higher viscosity compared with the base fluid and the accompanying higher velocity gradients. Besides, the effect gets more significant with the growth in *Re*. As shown in Figure 5d, the S_{rf} value increases due to nanofluids dramatically ascend when *Re* rises. It is caused by that with the increase in *Re*, the influence of the viscosity difference between the nanofluids with various volume fractions gradually gets more significant. Considering that the increase in S_{rf} value is not comparable to the decrease in S_{rh} value, as a consequence, the average total entropy generation rate S_{rgen} expresses a variation tendency with high similarity with that of S_{rh} as shown in Figure 5e. It is concluded that the S_{rgen} values dramatically decrease when *Re* rises or nanofluid volume fraction increases, and the effect of nanofluid on S_{rgen} gradually becomes inconspicuous with the growth in *Re* as shown in Figure 5f. Furthermore, it should be paid great attention to that with the increase in *Re*, the difference between S_{rh} value and S_{rf} value gets lower, so does the influences of nanofluids on these two values. Consequently, it can be predicted that the in the flow and heat transfer with *Re* higher than that in this paper, called critical *Re* here, the S_{rf} value will play a role as important as S_{rh} value in the effect on average total entropy generation rate. The detailed study on the critical *Re* will be considered in the further investigation.

3.2.2. Effect of Dimples/Protrusions on Entropy Generation

As to the comparison between the influences of dimple-case and protrusion-case, it can be seen from Figure 5a that the protrusion-case' S_{rh} values are much lower than those of dimple-case, especially in low *Re*. The difference between the S_{rh} values of protrusion-case and dimple-case gradually declines when *Re* rises, which is mainly caused by that in laminar flow, the protrusion-case's heat transfer enhancement capacity is markedly stronger than that of dimple-case, leading to the more uniform temperature field and lower temperature gradient. Consequently, the S_{rh} value is much lower. With the growth in *Re*, the turbulence's effect on heat transfer becomes increasingly remarkable and the influences of dimples and protrusions are relatively reduced. With regard to S_{rf}, it can be found in Figure 5c that the S_{rf} values of protrusion-case are distinctly higher than those of dimple-case at given Reynolds numbers, of which the difference increasingly ascends with the rise in *Re*, which is considered to be the result of that when *Re* rises, the effect of protrusion-case's flow separation on the flow field grows and the large flow separation region brings about the local low velocity region and the accompanying increase in local friction entropy generation rate.

It should be noted that after checking the results of all cases, the S_{rh} values and S_{rf} values in dimple-case are markedly lower than S_{rh0} and S_{rf0} at given Reynolds numbers, respectively, suggesting that dimple-case has great benefit in decreasing entropy generation compared to smooth channel both in heat transfer entropy generation rate and friction entropy generation rate, which primarily owes to the heat transfer enhancement by dimples without significant additional flow resistance. Besides, the protrusion-case also provides notable advantage in diminishing heat transfer entropy generation, of which the mechanism is similar to that in dimple-case. Nevertheless, the S_{rf} values in protrusion-case are considerably higher than S_{rf0}, which indicates that when compared with smooth channel, protrusion-case suffers from penalty of distinct friction entropy generation rate increase though it performs well in heat transfer entropy generation rate decline.

Furthermore, for a better understanding, the contours of S'''_{dh} and S'''_{df} are illustrated, here taking *Re* = 3000 as examples. Figure 6 provides the S'''_{dh} and S'''_{df} distributions on the spanwise-vertical plane (abbreviated as Plane 1) and streamwise-vertical plane (abbreviated as Plane 2) in both dimple-case and protrusion-case when *Re* = 3000, where the mainstream flows from the left to right in Plane 1. It is shown that S'''_{dh} keeps at a quite low level in the major area of the domain, and the high S'''_{dh} region is mainly located at the boundary layer near the wall where high temperature gradients exist, resulting in a high S'''_{dh} layer. It can be found that the thickness of the high S'''_{dh} layer in protrusion-case is evidently lower than that in the dimple-case, which is caused by the acceleration of the mainstream near the protrusion leading edge and the local reattachment. As shown in Figure 6c, part of the speeded mainstream intensively impinges on the opposite smooth wall and then the developments of the flow and heat boundary layers are both strongly disturbed. The local heat transfer is enhanced and lower temperature gradients are achieved. Nevertheless, the disturbance effect above in the dimple-case not as significant as that in protrusion-case, bringing about a thicker high S'''_{dh} layer. Besides, two symmetrical high S'''_{dh} regions are detected inside the dimple as shown in Figure 6b, which is caused by the corresponding local symmetrical vortex structures. Similarly, the symmetrical high S'''_{dh} regions found near the opposite smooth wall as shown in Figure 6d are also the results of local large vortices. With regard to S'''_{df}, it is shown that the high S'''_{df} regions are also principally located near the boundary layers. It can be seen from Figure 6e that there is a low S'''_{df} region near the dimple trailing edge which is distinctly different from the leading edge and the two lateral sides. It is a consequence of the local reattachment that disturbs the flow boundary layer development and then decreases the local velocity gradient. Furthermore, it is observed from Figure 6h that several high S'''_{df} regions are detected which are found to be in great accordance with the low velocity areas after checking the velocity distribution. Local flow separations give rise to the low velocity areas that increase the local velocity gradients, leading to the higher S'''_{df} values.

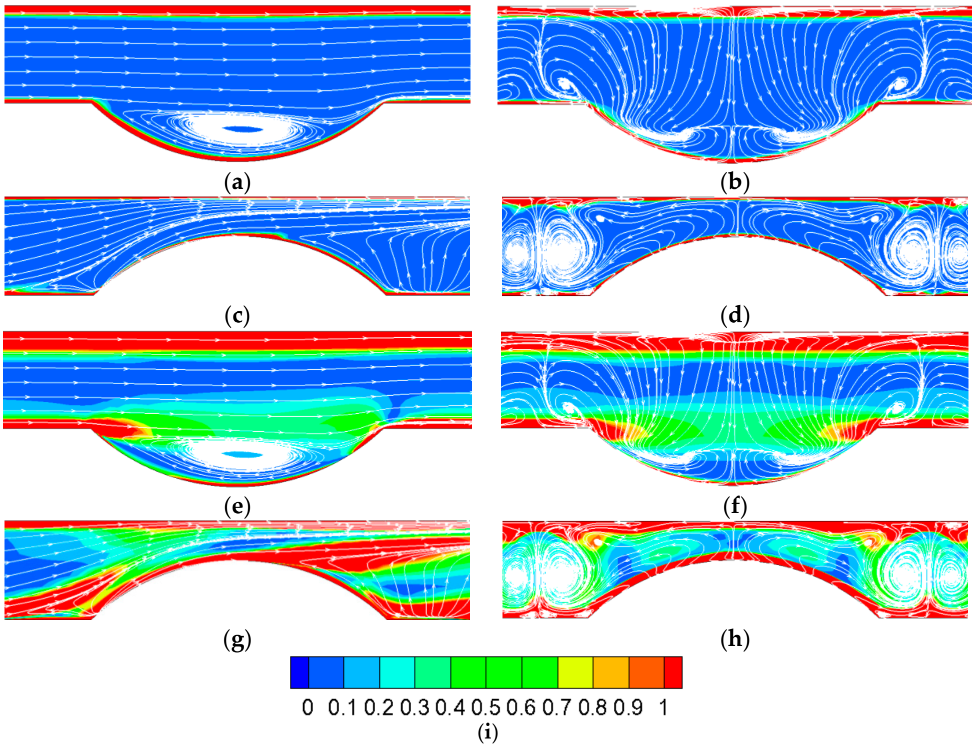

Figure 6. S'''_{dh} and S'''_{df} contours on spanwise-vertical plane and streamwise-vertical plane: (**a**) dimple-S'''_{dh}-Plane 1; (**b**) dimple-S'''_{dh}-Plane 2; (**c**) protrusion-S'''_{dh}-Plane 1; (**d**) protrusion-S'''_{dh}-Plane 2; (**e**) dimple-S'''_{df}-Plane 1; (**f**) dimple-S'''_{df}-Plane 2; (**g**) protrusion-S'''_{df}-Plane 1; and (**h**) protrusion-S'''_{df}-Plane 2; (**i**) color guide for (a–h).

3.3. Heat Transfer Performance Analysis

Taking the cases with Re = 3000 as examples for the heat transfer performance analysis, Figure 7 provides the wall temperature distributions and limit streamlines on the heated walls in dimple-case and protrusion-case, and the cases with ϕ = 0% and ϕ = 9% are selected to illustrate the effect of nanofluids, where the mainstream flows from the left to right. In dimple-case, it is shown that two symmetrical large vortices occur inside the dimple, leading to two symmetrical high temperature regions in agreement with the vortices' locations. The reattachment on the dimple trailing edge significantly enhances the local heat transfer, resulting in a large low temperature region. With the employment of nanofluids, the whole temperature distribution pattern hardly alters. Nevertheless, it is quite obvious that the high temperature regions' area notably decreases and the low temperature regions' area markedly increases. Moreover, the entire temperature level prominently declines almost at all regions when nanofluids is adopted, indicating the great enhancement of heat transfer, especially on the dimple trailing edge. The wall temperature distribution on the opposite smooth wall is also given in Figure 7c,d. It is found that there is a notable decrease in the area of the high temperature regions with the employment of nanofluid. In protrusion-case, the low temperature regions are mainly located at the protrusion leading edges, and the high temperature regions are substantially detected near the flow separation regions between the two rows of protrusions. The acceleration and impinging enhance the local heat transfer, which is deteriorated near the vortices. When nanofluids is employed, it is seen that the high temperature regions' area declines and the low temperature regions' area grows. The analogous effect also takes place on the opposite smooth wall, and the wall temperature level markedly drops.

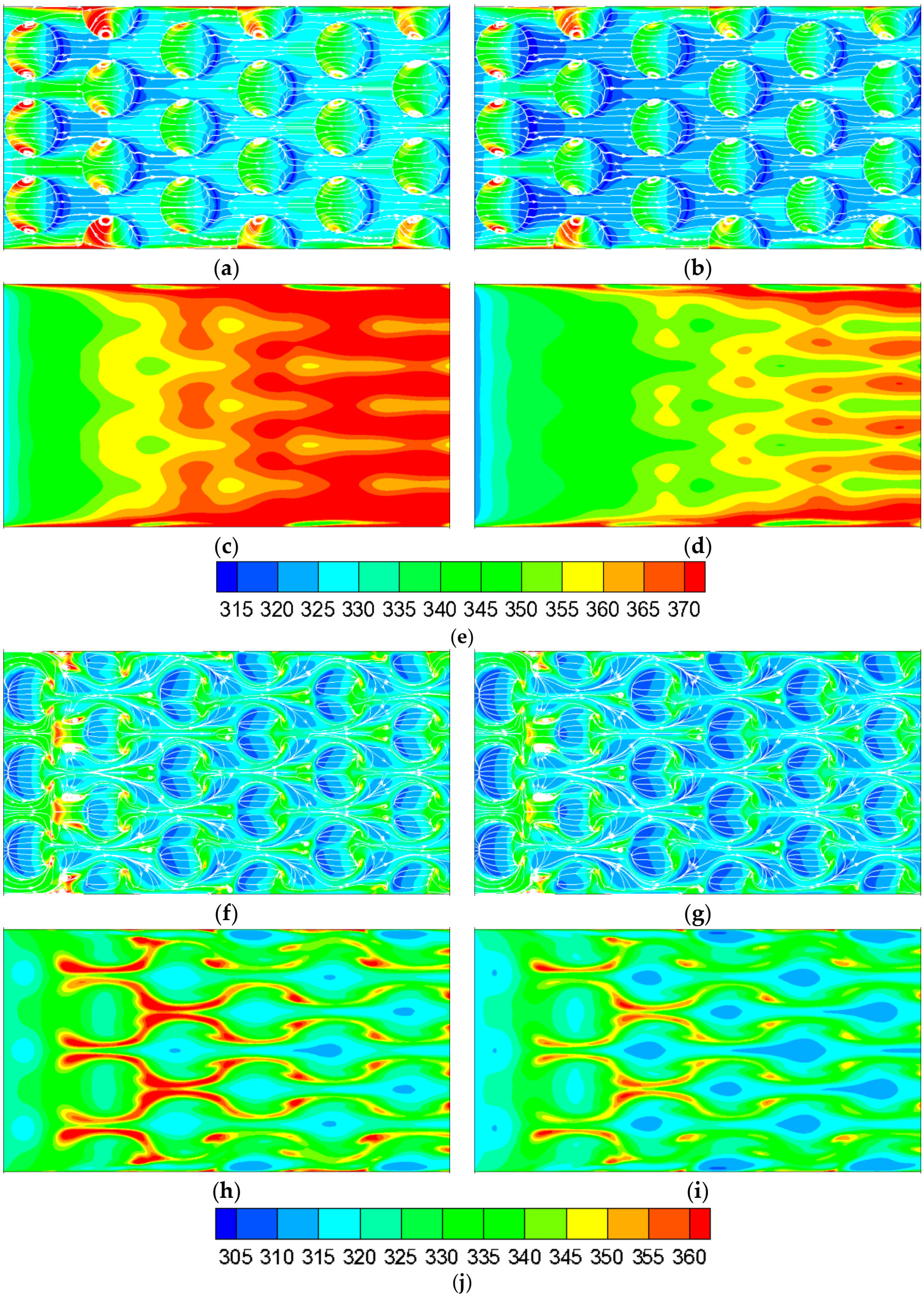

Figure 7. Wall temperature and limit streamlines on heated walls (units: K): (**a**) dimple-ϕ = 0%; (**b**) dimple-ϕ = 9%; (**c**) dimple-smooth wall-ϕ = 0%; (**d**) dimple-smooth wall-ϕ = 9%; (**e**) color guide for (a–d); (**f**) protrusion-ϕ = 0%; (**g**) protrusion-ϕ = 9%; (**h**) protrusion-smooth wall-ϕ = 0%; (**i**) protrusion-smooth wall-ϕ = 9%; (**j**) color guide for (f–i).

For a more comprehensive analysis, the variation tendencies of the average wall temperature T_w, wall temperature uniformity ΔT_s and pumping power *P.P versus Re* are provided in Figure 8. It can be found in Figure 8a that at a given *Re*, T_w keeps decreasing with the increase in nanofluids volume fraction in both dimple-case and protrusion-case, which is primarily due to the higher effective thermal conductivity. In other words, higher volume fraction brings about more effective cooling. Besides, the effect of nanofluids gradually gets weak when *Re* rises. In industrial application, the high temperature rise results in the nonuniform temperature distribution on the equipment that may bring about the damaging thermal stress as the consequence of the difference in thermal expansion coefficient. Besides, the spatial temperature gradient also has a negative effect on the equipment's stable operation. It is shown in Figure 8b that with the growth in *Re*, the temperature uniformity ΔT_s notably declines in both dimple-case and protrusion-case. Besides, the temperature uniformity also decrease with an increasing nanofluid volume fraction, indicating the improvement of temperature uniformity with the employment of nanofluid. It is found from Figure 8c that with the increase in volume fraction, the pumping power *P.P* ascends in both dimple-case and protrusion-case, which is mainly caused by the rise in the effective viscosity that results in a larger pressure drop. Moreover, the pumping power also grows with an increasing *Re* as expected.

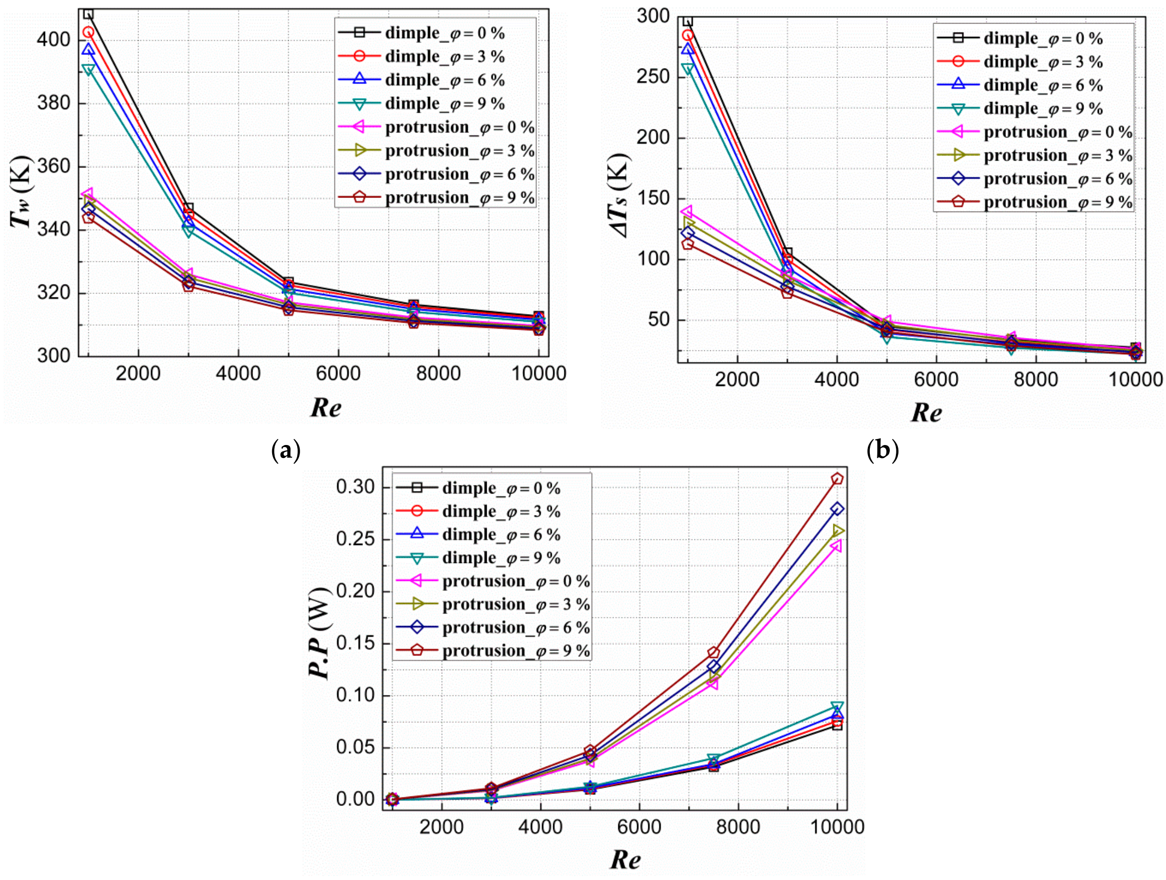

Figure 8. Average wall temperature, wall temperature uniformity and pumping power variation characteristics: (**a**) T_w *vs. Re*; (**b**) ΔT_s *vs. Re*; and (**c**) *P.P vs. Re.*

4. Conclusions

In this study, effect of Al_2O_3-water nanofluid flow on entropy generation and heat transfer performance in a rectangular conventional channel with staggered dimples and protrusions is numerically investigated. Some important conclusions from the results can be drawn as follows.

- When *Re* reaches 10,000 or even higher, the mainstream has completely turned into turbulent flow, and *Re* range in this study covers laminar flow, transitional flow and turbulent flow.
- The S_{rh} keeps decreasing at a given *Re* with an increasing volume fraction, and the decrease of the S_{rh} owing to nanofluids declines with the increase in *Re*. The employment of nanofluid increases S_{rf} at a given *Re*, and S_{rf} further ascends with an increasing volume fraction, in which the effect gets more significant with the growth in *Re*. The S_{rgen} expresses a variation tendency with high similarity with that of S_{rh} under the *Re* range in this study.
- The dimple-case has great benefit in decreasing entropy generation compared to smooth channel both in heat transfer entropy generation rate and friction entropy generation rate. The protrusion-case suffers from penalty of distinct friction entropy generation rate increase though it performs well in heat transfer entropy generation rate decline.
- The S'''_{dh} keeps at a quite low level in the major area of the domain, and the high S'''_{dh} regions are mainly located near the boundary layer and the local vortices. There is a low S'''_{df} region near dimple trailing edge, and high S'''_{df} regions are detected in accordance with low velocity areas.
- The high temperature regions' area notably decreases and the low temperature regions' area markedly increases with an increasing volume fraction. The entire temperature level prominently declines almost at all regions in both the structured and smooth surfaces.
- With the increase in nanofluids volume fraction, T_w keeps decreasing, ΔT_s declines and *P.P* ascends in both dimple-case and protrusion-case at a given *Re*.
- Conclusively, it is preferred to employ nanofluids to obtain great heat transfer enhancement performance and significant entropy generation decrease under laminar flow. It is also recommended that protrusions be adopted under laminar flow for its superior heat transfer enhancement performance and remarkable entropy generation decrease. Besides, dimples are preferable under turbulent flow in order to avoid high pumping power and excessive friction entropy generation increase.

Author Contributions: Yonghui Xie and Lu Zheng performed the numerical simulations, finished the results analysis, and then wrote some sections of the manuscript. Di Zhang and Gongnan Xie prepared some other sections of the paper. All of the authors contributed equally for reviewing and revising the manuscript. All authors have read and approved the final manuscript.

Conflicts of Interest: The authors declare no conflict of interest.

Abbreviations

The following abbreviations are used in this manuscript:

A	wall area (m^3)
C_p	specific heat (J/kg·K)
D	dimple/protrusion print diameter (m)
D_h	hydraulic diameter (m)
f	resistance coefficient
H	channel height (m)
k	thermal conductivity (W/m· K)
L	heated section length (m)
M	mass flow rate (kg/s)
Nu	Nusselt number
$P.P$	pumping power (W)
Re	Reynolds number
S'''_{gen}	local total entropy generation rate (W/m^3· K)
S'''_h	local heat transfer entropy generation rate (W/m^3· K)
S'''_f	local friction entropy generation rate (W/m^3· K)

S'''_{dgen}	dimensionless local total entropy generation rate
S'''_{dh}	dimensionless local heat transfer entropy generation rate
S'''_{df}	dimensionless local friction entropy generation rate
S_{rgen}	average total entropy generation rate (W/m^3· K)
S_{rh}	average heat transfer entropy generation rate (W/m^3· K)
S_{rf}	average friction entropy generation rate (W/m^3· K)
S_{rh0}	average heat transfer entropy generation rate of smooth channel (W/m^3· K)
S_{rf0}	average friction entropy generation rate of smooth channel (W/m^3· K)
T_w	wall temperature (K)
$U_{m,in}$	inlet average velocity (m/s)
W	channel height (m)
x, y, z	Cartesian coordinates (m)
Greek Characters	
δ	dimple/protrusion depth (m)
ϕ	volume fraction (%)
γ	turbulence intermittency
ρ	density (kg/m^3)
μ	viscosity (Pa· s)
ΔT_s	temperature uniformity (K)
ΔP	pressure drop (Pa)
Subscripts	
max	maximum value
min	minimum value
nf	nanofluid
f	basefluid
p	nanoparticle
in	inlet

References

1. Choi, U.S.; Eastman, J.A. Enhancing thermal conductivity of fluids with nanoparticles. In Proceedings of the 1995 International Conference on Mechanical Engineering Congress and Exhibition, San Francisco, CA, USA, 12–17 November 1995.
2. Saidur, R.K.; Leong, Y.; Mohammad, H.A. A review on applications and challenges of nanofluids. *Renew. Sustain. Energy Rev.* **2011**, *15*, 1646–1668. [CrossRef]
3. Hadad, Z.; Oztop, H.F.; Abu-Nada, E.; Mataoui, A. A review on natural convective heat transfer of nanofluids. *Renew. Sustain. Energy Rev.* **2012**, *16*, 5363–5378. [CrossRef]
4. Khanafer, K.; Vafai, K. A critical synthesis of thermophysical characteristics of nanofluids. *Int. J. Heat Mass Transf.* **2011**, *54*, 4410–4428. [CrossRef]
5. Mahbubul, I.M.; Saidur, R.; Amalina, M.A. Latest developments on the viscosity of nanofluids. *Int. J. Heat Mass Transf.* **2012**, *55*, 874–885. [CrossRef]
6. Fan, J.; Wang, L. Review of heat conduction in nanofluids. *J. Heat Transf.* **2011**, *133*, 040801. [CrossRef]
7. Brinkman, H.C. The viscosity of concentrated suspensions and solutions. *J. Chem. Phys.* **1952**, *20*, 571. [CrossRef]
8. Corcione, M. Heat transfer features of buoyancy-driven nanofluids inside rectangular enclosures differentially heated at the sidewalls. *Int. J. Therm. Sci.* **2010**, *49*, 1536–1546. [CrossRef]
9. Duangthongsuk, W.; Wongwises, S. Measurement of temperature-dependent thermal conductivity and viscosity of TiO_2-water nanofluids. *Exp. Therm. Fluid Sci.* **2009**, *33*, 706–714. [CrossRef]
10. Maxwell, J.C. *A Treatise Electricity Magnetism*, 2nd ed.; Clarendon Press: Oxford, UK, 1881.
11. Bruggeman, D.A.G. Berechnung verschiedener physikalischer Konstanten von heterogenen Substanzen. I. Dielektrizitatskonstanten und Leitfahigkeiten der Mischkorper aus isotropen Substanzen. *Annalen der Physik* **1935**, *416*, 636–664. (In German) [CrossRef]

12. Hamilton, R.L.; Crosser, O.K. Thermal conductivity of heterogeneous two component systems. *Ind. Eng. Chem. Fundam.* **1962**, *1*, 182–191. [CrossRef]
13. Nan, C.W.; Birringer, R.; Clarke, D.R.; Gleiter, H. Effective thermal conductivity of particulate composites with interfacial thermal resistance. *J. Appl. Phys.* **1997**, *81*, 6692–6699. [CrossRef]
14. Yu, W.; Choi, S.U.S. The role of interfacial layers in the enhanced thermal conductivity of nanofluids: A renovated Maxwell model. *J. Nanopart. Res.* **2003**, *5*, 167–171. [CrossRef]
15. Yu, W.; Choi, S.U.S. The role of interfacial layers in the enhanced thermal conductivity of nanofluids: A renovated Hamilton–Crosser model. *J. Nanopart. Res.* **2004**, *6*, 355–361. [CrossRef]
16. Koo, J.; Kleinstreuer, C. A new thermal conductivity model for nanofluids. *J. Nanopart. Res.* **2004**, *6*, 577–588. [CrossRef]
17. Feng, Y.; Kleinstreuer, C. Nanofluid convective heat transfer in a paralleldisk system. *Int. J. Heat Mass Transf.* **2010**, *53*, 4619–4628. [CrossRef]
18. Machrafi, H.; Lebon, G. The role of several heat transfer mechanisms on the enhancement of thermal conductivity in nanofluids. *Contin. Mech. Thermodyn.* **2016**. [CrossRef]
19. Seyf, H.R.; Feizbakhshi, M. Computational analysis of nanofluid effects on convective heat transfer enhancement of micro-pin-fin heat sinks. *Int. J. Therm. Sci.* **2012**, *58*, 168–179. [CrossRef]
20. Selvakumar, P.; Suresh, S. Convective performance of CuO/water nanofluid in an electronic heat sink. *Exp. Therm. Fluid Sci.* **2012**, *40*, 57–63. [CrossRef]
21. Diao, Y.H.; Liu, Y.; Wang, R.; Zhao, Y.H.; Guo, X.; Tang, X. Effects of nanofluids and nanocoatings on the thermal performance of an evaporator with rectangular microchannels. *Int. J. Heat Mass Transf.* **2013**, *67*, 183–193. [CrossRef]
22. Wen, D.S.; Ding, Y.L. Experimental investigation into convective heat transfer of nanofluids at the entrance region under laminar flow conditions. *Int. J. Heat Mass Transf.* **2004**, *47*, 5181–5188. [CrossRef]
23. Suresh, S.; Chandrasekar, M.; Selvakumar, P. Experimental studies on heat transfer and friction factor characteristics of CuO/water nanofluid under laminar flow in a helically dimpled tube. *Heat Mass Transf.* **2012**, *48*, 683–694. [CrossRef]
24. Suresh, S.; Chandrasekar, M.; Chandra Sekhar, S. Experimental studies on heat transfer and friction factor characteristics of CuO/water nanofluid under turbulent flow in a helically dimpled tube. *Exp. Therm. Fluid Sci.* **2011**, *35*, 542–549. [CrossRef]
25. Vakili, M.; Mohebbi, A.; Hashemipour, H. Experimental study on convective heat transfer of TiO_2 nanofluids. *Heat Mass Transf.* **2013**, *49*, 1159–1165. [CrossRef]
26. Xuan, Y.M.; Li, Q. Investigation on Convective Heat Transfer and Flow Features of Nanofluids. *ASME J. Heat Transf.* **2003**, *125*, 151–155. [CrossRef]
27. Gavili, A.; Isfahani, T.D.; Zabihi, F.; Hadi, I. The effect of real viscosity on the heat transfer of water based Al_2O_3 nanofluids in a two-sided lid-driven differentially heated rectangular cavity. *Heat Mass Transf.* **2013**, *49*, 1433–1445. [CrossRef]
28. Mohammed, H.A.; Al-Shamani, A.N.; Sheriff, J.M. Thermal and hydraulic characteristics of turbulent nanofluids flow in a rib–groove channel. *Int. Commun. Heat Mass Transf.* **2012**, *39*, 1584–1594. [CrossRef]
29. Oztop, H.F.; Al-Salem, K. A review on entropy generation in natural and mixed convection heat transfer for energy systems. *Renew. Sustain. Energy Rev.* **2012**, *16*, 911–920. [CrossRef]
30. Singh, P.K.; Anoop, K.B.; Sundararajan, T.; Das, S.K. Entropy generation due to flow and heat transfer in nanofluids. *Int. J. Heat Mass Transf.* **2010**, *53*, 4757–4767. [CrossRef]
31. Li, J.; Kleinstreuer, C. Entropy generation analysis for nanofluid flow in microchannels. *J. Heat Transf.* **2010**, *132*, 122401. [CrossRef]
32. Moghaddami, M.; Mohammadzade, A.; Varzane Esfehani, S.A. Second law analysis of nanofluid flow. *Energy Convers. Manag.* **2011**, *52*, 1397–1405. [CrossRef]
33. Leong, K.Y.; Saidur, R.; Mahlia, T.M.I.; Yau, Y.H. Entropy generation analysis of nanofluid flow in a circular tube subjected to constant wall temperature. *Int. Commun. Heat Mass Transf.* **2012**, *39*, 1169–1175. [CrossRef]
34. Mahian, O.; Mahmud, S.; Zeinali Heris, S. Analysis of entropy generation between co-rotating cylinders using nanofluids. *Energy* **2012**, *44*, 438–446. [CrossRef]
35. Shahi, M.; Mahmoudi, A.H.; Raouf, A.H. Entropy generation due to natural convection cooling of a nanofluid. *Int. Commun. Heat Mass Transf.* **2011**, *38*, 972–983. [CrossRef]

36. Mahmoudi, A.H.; Talebi, F.; Shahi, M. Entropy generation due to natural convection cooling of a horizontal heat source mounted inside a square cavity filled with nanofluid. *Heat Transf. Res.* **2012**, *43*, 19–46.
37. Khorasanizadeh, H.; Nikfar, M.; Amani, J. Entropy generation of Cu–water nanofluid mixed convection in a cavity. *Eur. J. Mech. B Fluids* **2013**, *37*, 143–152. [CrossRef]
38. Khorasanizadeh, H.; Nikfar, M.; Amani, J. Numerical investigation of Cu–water nanofluid natural convection and entropy generation within a cavity with an embedded conductive baffle. *Sci. Iran* **2012**, *19*, 1996–2003. [CrossRef]
39. Esmaeilpoura, M.; Abdollahzadeh, M. Free convection and entropy generation of nanofluid inside an enclosure with different patterns of vertical wavy walls. *Int. J. Therm. Sci.* **2012**, *52*, 127–136. [CrossRef]
40. Cho, C.C.; Chen, C.L.; Chen, C.K. Natural convection heat transfer and entropy generation in wavy-wall enclosure containing water-based nanofluid. *Int. J. Heat Mass Transf.* **2013**, *61*, 749–758. [CrossRef]
41. Boghrati, M.; Bajestan, E.E.; Etminan, V. Entropy generation minimization of confined nanofluids laminar flow around a block. In Proceedings of the ASME 10th Biennial Conference on Engineering Systems and Analysis, Istanbul, Turkey, 12–14 July 2010.
42. Sarkar, S.; Ganguly, S.; Dalal, A. Analysis of entropy generation during mixed convection heat transfer of nanofluids past a square cylinder in vertically upward flow. *J. Heat Transf.* **2012**, *134*, 122501. [CrossRef]
43. Leong, K.Y.; Saidur, R.; Khairulmaini, M.; Michael, Z.; Kamyar, A. Heat transfer and entropy analysis of three different types of heat exchangers operated with nanofluids. *Int. Commun. Heat Mass Transf.* **2012**, *39*, 838–843. [CrossRef]
44. Matin, M.H.; Nobari, M.R.H.; Jahangiri, P. Entropy analysis in mixed convection MHD flow of nanofluid over a non-linear stretching sheet. *J. Therm. Sci. Technol.* **2012**, *7*, 104–119. [CrossRef]
45. Selimefendigil, F.; Oztop, H.F.; Abu-Hamdeh, N. Natural convection and entropy generation in nanofluid filled entrapped trapezoidal cavities under the influence of magnetic field. *Entropy* **2016**, *18*, 43. [CrossRef]
46. Menter, F.R. Two-equation eddy-viscosity turbulence models for engineering applications. *AIAA J.* **1994**, *32*, 1598–1605. [CrossRef]
47. Menter, F.R.; Langtry, R.B.; Likki, S.R.; Suzen, Y.B.; Huang, P.G.; Volker, S. A correlation-based transition model using local variables—Part I: Model formulation. *J. Turbomach.* **2006**, *128*, 413–422. [CrossRef]
48. Manca, O.; Mesolella, P.; Nardini, S.; Ricci, D. Numerical study of a confined slot impinging jet with nanofluids. *Nanoscale Res. Lett.* **2011**, *6*, 1–16. [CrossRef] [PubMed]
49. Ho, C.J.; Chen, M.W.; Li, Z.W. Numerical simulation of natural convection of nanofluid in a square enclosure: Effects due to uncertainties of viscosity and thermal conductivity. *Int. J. Heat Mass Transf.* **2008**, *51*, 4506–4516. [CrossRef]
50. Bejan, A. *Entropy Generation through Heat and Fluid Flow*; Wiley: New York, NY, USA, 1982.
51. Gnielinski, V. New equations for heat transfer in turbulent pipe and channel flows. *Int. Chem. Eng.* **1976**, *16*, 359–368.
52. Shah, R.K.; London, A.L. *Laminar Flow Forced Convection in Ducts: A Source Book for Compact Heat Exchanger Analytical Data*; Academic Press: New York, NY, USA, 1978.
53. Flionenko, G.K. Hydraulic Resistance in Pipes. *Teploenergetika* **1954**, *1*, 40–44. (In Russian)